Topography and motion of the acid-sensing ion channel intracellular domains

Tyler Couch[1], Kyle Berger[2], Dana L. Kneisley[2], Tyler W. McCullock[1], Paul J. Kammermeier[2] and David M. MacLean[2]*

[1]Graduate Program in Cellular and Molecular Pharmacology and Physiology

[2]Department of Pharmacology and Physiology, University of Rochester Medical Center

*To whom correspondence should be addressed

Keywords: ASIC, FRET, gating, patch clamp fluorometry, DPA, fluorescence

1 **Abstract**

2 Acid-sensing ion channels (ASICs) are trimeric cation-selective channels activated by

3 decreases in extracellular pH. The intracellular N and C terminal tails of ASIC1 influence

4 channel gating, trafficking, and signaling in ischemic cell death. Despite several x-ray and

5 cryo-EM structures of the extracellular and transmembrane segments of ASIC1, these

6 important intracellular tails remain unresolved. Here we describe the coarse topography

7 of the cASIC1 intracellular domains determined by FRET, measured using either

8 fluorescent lifetime imaging or patch clamp fluorometry. We find the C terminal tail

9 projects into the cytosol by approximately 35 Å and that the N and proximal segment of

10 the C tail from the same subunits are closer than adjacent subunits. Using pH-insensitive

11 fluorescent proteins, we fail to detect any relative movement between the N and C tails

12 upon extracellular acidification but do observe axial motions of the membrane proximal

13 segments towards the plasma membrane. Taken together, our study furnishes a coarse

14 topographic map of the ASIC intracellular domains while providing directionality and

15 context to intracellular conformational changes induced by extracellular acidification.

1 **Introduction**

2   The predominant sensor of extracellular pH in the central and peripheral nervous

3 system is thought to be acid-sensing ion channels (ASICs)[1]. This family of trimeric pH-

4 activated sodium-selective ion channels couples extracellular acidification to numerous

5 physiological and pathophysiological consequences including synaptic transmission and

6 plasticity[2-6], fear memory consolidation and expression[7-10], epilepsy[11] and ischemia-

7 induced cell death[12,13]. However, in many of these cases the duration of extracellular

8 acidosis is quite long. Since most ASIC subunits desensitize nearly completely in a few

9 seconds[14,15], how might these channels convey information over minutes or hours? While

10 other extracellular pH sensors may play roles[1,16], recent evidence reveals that ASICs

11 possess both canonical ionic and non-canonical metabotropic signaling capabilities.

12   Extracellular acidosis is proposed to drive the association of the serine/threonine

13 kinase receptor interacting protein 1 (RIP1) and N-ethylmaleimide-sensitive factor (NSF)

14 with ASIC1a, triggering RIP1 phosphorylation and initiating a necroptotic signaling

15 cascade[17,18]. This occurs independent of ASIC1a ion conductance and via intracellular

16 protein-protein interactions[17,18]. Thus, ASICs join a growing, and controversial, list of

17 ligand-gated ion channels who also possess metabotropic signaling capacity[19-23]. Like

18 many of these ion channels, the structure of the ASIC extracellular and transmembrane

19 regions have been determined[24-27] but the intracellular domains are unresolved. It is likely

20 that the ASIC intracellular domains (ICDs) are partly, or even mostly, unstructured

21 regions. Nonetheless, understanding the coarse outline of the two ICDs, the N and C tails,

22 as well as their pH-induced movements, would inform further investigation of ASIC

23   metabotropic signaling and may shed light on how the ICDs impact gating, protein-protein

24   interactions and/or trafficking[28-34].

25   Here we set out to generate a coarse topography of the cASIC1 intracellular N and

26   C termini using FRET in several configurations. We find that the short (15 amino acid) N

27   tail projects about 6-10 angstroms from the membrane inner leaflet into the cytosol while

28   the longer 67 amino acid C tail extends between 30 to 40 angstroms. This contrasts with

29   the unresolved tail of AMPA receptors that is largely perpendicular to the membrane[35].

30   We also report that the N and proximal segment of the C tail from the same subunits are

31   closer than adjacent subunits, suggesting preferential intra-subunit tail interactions which

32   may inform the interpretation of experiments with heteromeric channels. Finally, using

33   pH-insensitive fluorescent proteins, we fail to detect any relative movement between the

34   N and C tails but do observe axial motions of these segments towards the plasma

35   membrane upon extracellular acidification. Together, these data allow us to build a

36   topographical model of the intracellular tails of ASIC1 that will be a foundation for working

37   hypotheses in future experiments.

38

Materials and Methods

Plasmids and molecular cloning

A pcDNA3.1(+) vector containing the sequence for codon-optimized chicken ASIC1 (pcDNA3.1-cocASIC1) was used for all experiments[36]. Scar-less insertion of fluorescent protein tags was achieved by opening the pcDNA3.1-cocASIC1 vector by PCR with primers containing 18-nt homologous overhangs. Fluorescent protein sequences were PCR-derived from pmVenus(L68V)-mTurquiose2 (Addgene plasmid #60493), Gamillus/pcDNA3 (Addgene plasmid #124837), or PSD-95-pTagRFP (Addgene #52671), and cloned in using NEBuilder HiFi DNA Assembly Master Mix (New England Biolabs) according to the manufacturer's instructions. These fluorescent protein constructs were gifts from Dorus Gadella, Takeharu Nagai, and Johannes Hell, respectively. All constructs were verified by Sanger sequencing (Eurofins Genomics). The Lck membrane tether clones were made using Lck-mScar-I (Addgene #98821), removing the mScarlet by inverse PCR and inserting PCR derived mTurquiose2 or mVenus. Throughout the manuscript CFP, GFP, YFP and RFP to refer to mTurquoise2, Gamillus, mVenus and TagRFP, respectively.

Cell culture and transfection

A clonal Human Embryonic Kidney 293T (HEK293T) cell line with the endogenous ASIC1 gene knocked out were used for all experiments[37]. HEK293T cells were maintained in Minimum Essential Medium (MEM) containing glutamine and Earle's salts (Gibco) supplemented with 10% fetal bovine serum (Atlas Biologicals) and PenStrep (Gibco). Cells were plated in 35-mm tissue culture treated dishes and transfected 1-2 days later using polyethylenimine 25k (Polysciences, Inc) with a mass ratio of 1:3

62   (cDNA:PEI). For DPA quenching experiments, 500 ng of pcDNA3.1-cocASIC1 with a

63   fluorescent protein tag and 2.0 µg of pcDNA3.1(+)-empty vector were co-transfected per

64   35 mm dish. We found that dilution with the empty vector helped limit intracellular

65   accumulation of the channel. Cells were dissociated 24 to 48-hours post-transfection with

66   divalent-free DPBS (Gibco) supplemented with 0.5 mM EDTA and sparsely seeded onto

67   18 mm No 1 coverslips that had been treated with 100 ug/mL poly-lysine for 20 minutes.

68   *Electrophysiology*

69   Excised patch recordings were done as described previously[36]. Briefly, borosilicate patch

70   pipettes were pulled and heat-polished to a resistance of 3-6 MΩ. The internal pipette

71   solution was (in mM) 135 CsF, 11 EGTA, 10 HEPES, 10 MES, 2 $MgCl_2$, 1 $CaCl_2$, and pH

72   adjusted to 7.4 using CsOH. External solutions were comprised of (in mM) 150 NaCl, 1

73    $CaCl_2$, 1 $MgCl_2$, and either 20 HEPES (pH 8.0) or 20 MES (pH 5.0) and adjusted using

74   NaOH. Data were acquired at 20-50 kHz and filtered online at 10 kHz using AxoGraph

75   software (Axograph), an Axopatch 200B amplifier (Molecular Devices) and USB-6343

76   DAQ (National Instruments) at room temperature and with a holding potential of -60 mV.

77   Series resistance was routinely compensated by 90-95% when the peak amplitude

78   exceeded 100 pA. A home built double or triple barrel perfusion pipette[38] (Vitrocom)

79   attached to a piezo translator (Physik Instrumente) under computer control was used for

80   fast perfusion. Piezo voltage commands were generally filtered between 50 and 100 Hz.

81   *Patch clamp fluorometry*

82   Coverslips were visualized using a S Fluor 40x oil-immersion objective (N.A. 1.30,

83   Nikon) mounted on a Nikon Ti2 microscope. Transfected cells were excited and visualized

84   with either a 4-channel LED or single channel LED (Thorlabs) and dichroic filter cube.

85   Single cells were patched in a whole-cell configuration using heat-polished borosilicate

86   glass pipettes with 3-6 MΩ resistance. Cells were continually perfused with external

87   solution, with or without 5 µM dipicrylamine (Biotium), using a homebuilt multi-barrel flow

88   pipe (see above). Single cell fluorescence was collected using a D-104 dual channel

89   photometer (Photon Technology International) attached to the left microscope port.

90   Emitted fluorescence was limited to only the patched cell using adjustable slits and

91   detected with photomultiplier tubes (Hamamatsu Photonics, R12829). Photometers were

92   generally set to a voltage of 650-900 V and filtered with a time constant of 0.5 ms. The

93   photometer voltage signals were fed to the analog inputs of the same DAQ as the patch

94   clamp amplifier and recorded using AxoGraph. The timing of the excitation source was

95   triggered by TTL.

96   For DPA quenching experiments with CFP, a 455 nm LED, 455/20 nm excitation

97   filter, 442 nm dichroic and 510/84 nm emission filter were used. For YFP, a 505 nm LED,

98   510/20 excitation filter, 525 dichroic, and 545/35 band-pass emission filter were used. In

99   all cases, we worked to minimize background fluorescence by selecting cells with

100   prominent plasma membrane fluorescence and minimal intracellular signal. Quenching

101   curves were generated in whole cell configuration by a series of 100 ms steps ranging

102   from -180 to + 120 mV in 30 mV increments, with -15 mV holding potential and 1 second

103   between steps. Excitation was triggered 50 ms before a voltage step and lasted for 200

104   ms. This family of voltage steps was repeated four times either in control, with continual

105   perfusion of 5 µM DPA, or during DPA washes with several seconds separating each

106   condition. We found the data from the first family of DPA steps tended to be inconsistent,

107   presumably reflecting DPA equilibration within the cell. Thus, only the final 3 series of

108   steps were averaged together. For each recording a background signal was measured

109   by slightly moving the stage to a region with no cells and this signal subtracted. Analysis

110   was done using Clampfit (Molecular Devices) where, following background subtraction,

111   the average fluorescence signal in the second 20 ms window within the voltage step was

112   divided by the fluorescence signal at the preceding holding potential to generate F/F_{-15mV}.

113   These values for were plotted in OriginLab (OriginLab Corp) and cells were individually

114   fitted with a Boltzmann function. The difference of the minimum and maximum values of

115   the Boltzmann gave the $\Delta F/F_{-15mv}$ for that specific cell.

116   For patch clamp FRET experiments, the fluorescence emission was split into two

117   photomultiplier tubes. For CFP/YFP, a 455 nm LED, 455/20 nm excitation, 442 nm

118   dichroic, and 510/84 nm wide-band emission was used. This combination of donor and

119   acceptor emission was passed to the dual photometer, through the adjustable aperture,

120   and split by a 518 nm dichroic before further filtering into nominal donor (482/25 nm) and

121   acceptor (537/26 nm) emission channels. A similar configuration was used for GFP/RFP

122   with 455 nm LED, 470/10 nm excitation, 495 nm dichroic, 500 nm long-pass emission

123   followed by a 552 nm splitter diving donor (510/42 nm) and acceptor (609/54 nm). Single

124   cells were patch clamped and piezo-driven perfusion used to switch between pH 8.0, pH

125   7 and 6.0 for 2 seconds, with 20 seconds between acidic applications. The excitation

126   source was triggered 1 second before the solution switch for 10 seconds. The background

127   subtracted 'acceptor' channel fluorescence signal was divided by the subtracted 'donor'

128   channel signal to yield an apparent FRET signal. The goal of this experiment was to

129   ascertain if any changes in FRET are detectable upon activation/desensitization of the

130   channel, not to quantify the FRET efficiency. Therefore, we made no attempt to correct

131   for bleedthrough excitation or emission. To reflect this, all such measurements are

132   referred to as $\Delta FRET_{app}$ or change in apparent FRET.

133   *Fluorescence lifetime imaging and confocal imaging*

134   Fluorescent lifetime imaging (FLIM) was done as described previously[39]. Cells

135   were transfected in either 35mm or 60 mm culture dishes and imaged using a water

136   immersion 25x objective (XL Plan N, 1.05 NA) mounted on an Olympus IX61WI upright

137   microscope. A Mai Tai Sapphire multi-photon laser (Spectra Physics) was used for

138   excitation with an 860 nm wavelength, a repetition rate of 80 MHz and pulse width of ~

139   100 fs. Donor emission was filtered by a 480-20 filter and measured by a H72422P

140   Hamamatsu hybrid avalanche photodiode (APD). Time-correlated single photon counting

141   (TCSPC) was done using a Becker and Hickl card with a resolution of 25 ps. Using

142   VistaVision software (ISS), donor fluorescence from the plasma membrane from

143   individual cells was binned and fit with a single exponential function, consistent with the

144   lifetime of CFP variant mTurquoise2[40].

145   For confocal imaging, cells were transfected with Lck-CFP or CFP-tagged cASIC1

146   in 35 mm dishes. After two days, cells were stained with 2 mL of 7.5 µM FM1-43

147   (Invitrogen) immediately prior to imaging with an Olympus FV1000MP microscope using

148   a 60x water immersion objective (U Plan SApo, 1.20 NA). CFP and FM1-43 were

149   simultaneously excited with a 440 nm laser and emissions between 465-495 nm collected

150   as CFP and 575-675 nm collected as FM1-43.

151   *DPA quenching simulations*

152   Closely following the work of Wang[41] and Zachariassen[35], we calculated the FRET

153   between a donor fluorophore and a plane of DPA molecules over a range of axial

154   distances. The donor fluorophore was positioned at a distance, R_a, from a point within a

155   perpendicular plane representing the inner leaflet of the plasma membrane. This point is

156   the center of a ring of radius r, within the perpendicular plane. The distance between the

157   donor and DPA on the perimeter of the ring is the hypotenuse of a triangle with the other

158   sides being the ring radius, r, and the axial distance between the center of the ring and

159   the donor, R_a. Thus the donor-acceptor distance is $\sqrt{R_a^2 + r^2}$. We define $P(r)$ as the

160   probability that no FRET will occur between the donor and DPA positioned along ring

161   perimeter and $Q(r)$ as the probability FRET (quenching) will occur. As the sum of $P(r)$

162   and $Q(r)$ is one, for a ring of slightly larger radius $r + dr$

163     $$P(r + dr) = P(r)(1 - Q(r)dr)$$

164   FRET efficiency, E, over a distance, d, for a single donor-acceptor pair is given by

165     $$E = \frac{1}{1 + \left(d/R_0\right)^6}$$

166   Where R_0 is the Förster distance giving half-maximal FRET. As with past work, we used

167   5 µM DPA which gives a density, σ, of 1.25 x 10^{-4} molecules per Å^{-2} [41]. Combing the DPA

168   density and distance constraint we define the probability of quenching as

169     $$Q(r)dr = \frac{\sigma\, 2\pi\, r\, dr}{1 + \left(\dfrac{R_a^2 + r^2}{R_0^2}\right)^3}$$

170   Given equation 1, the following differential equation can be derived:

171     $$\frac{dP}{dr} = \frac{\sigma\, 2\pi\, r\, P}{1 + \left(\dfrac{R_a^2 + r^2}{R_0^2}\right)^3}$$

172   Substituting $u = (R_a^2 + r^2)/R_0^2$ and evaluating the integral at $r = \infty$ gives:

173
$$P_\infty = exp\left(-\sigma\pi R_0^2 \int_{\frac{R_a^2}{R_0^2}}^{\infty} \frac{du}{1 + u^3}\right)$$

174 Which represents the unquenched fluorescence signal remaining over a range of axial

175 distances. As DPA is assumed to traverse about 25 Å in the plasma membrane[35,41],

176 evaluating this integral using either R_a or $R_a + 25$ gives the quenching curves for DPA at

177 the inner leaflet or outer leaflet, which are populated by infinitely depolarizing or

178 hyperpolarizing conditions, respectively. R_0 calculations were done with the $k^2 = 2/3$

179 assumption, using donor fluorescent protein (FP) spectra and quantum yield listed in FP

180 database[42]. The DPA absorption spectrum was measured with 25 µM DPA diluted in

181 saline on a QuickDrop spectrophotometer (Molecular Devices). The DPA molar extinction

182 coefficient was determined to be 26,500 $M^{-1}cm^{-1}$ by fitting the slope of absorption

183 measurements from serial dilutions of DPA into saline or 1% SDS. This value is consistent

184 with previously reported measurements[43].

185 *Statistics and Data Analysis*

186 Current desensitization decays were fitted using exponential decay functions in

187 Clampfit (Molecular Devices). For recovery from desensitization experiments, the test

188 peak (i.e., the second response) was normalized to the conditioning peak (i.e., the first

189 response). OriginLab (OriginLab Corp) was used to fit the normalized responses to:

190
$$I_t = \left(1 - e^{(-t/\tau)}\right)^m \qquad\qquad \text{Eq. 1}$$

191 Where I_t is the fraction of the test peak at an interpulse interval of t compared to the

192 conditioning peak, τ is the time constant of recovery and m is the slope of the recovery

193 curve. Patches were individually fit and averages for the fits were reported in the text. N

194 was taken to be a single patch.

195   FRET efficiency from FLIM measurements was calculated using:

196
$$FRET_{efficiency} = 1 - \left({}^{\tau_{donor+acceptor}} / {}_{\tau_{donor\ only}} \right)$$

197   Where $\tau_{donor\ only}$ and $\tau_{donor+acceptor}$ are the single exponential time constants of donor decay

198   in the absence and presence of acceptor, respectively.

199   Unless otherwise noted, statistical testing was done using nonparametric

200   permutation or randomization tests with at least 100,000 iterations implemented in Python

201   to assess statistical significance.

202 **Results**

203 *Voltage-dependent quenching measurements with DPA*

204   The intracellular components of the cASIC1 N and C terminal tails are 15 and 67 amino

205 acids, respectively. The range of possible structures adoptable by these tails is quite large. For

206 example, in principle the C tail could exist as a linear strand of peptide more than 70 Å long[44]

207 extended parallel to the plasma membrane or as a similar extended strand but perpendicular to

208 the membrane plane, projecting 'downward' into the cytosol. These two extreme scenarios

209 represent the borders of the conformational landscape. The main goal of our study was to

210 experimentally shrink the range of possibilities and map this landscape. Our secondary goal was

211 to determine if these intracellular domains move upon extracellular acidification. To do this, we

212 adopted a FRET approach using different colored fluorescent proteins as donors and the

213 membrane soluble small molecule DPA as an acceptor (Figure 1A). DPA has several

214 advantageous properties as a FRET acceptor[41,45]. First, it is a dark acceptor, allowing FRET to

215 be easily measured by changes in donor emission. Second, it binds and dissociates from the

216 plasma membrane quickly with respect to the time of a patch clamp experiment. Third, and most

217 critically, the anionic DPA orients in the plasma membrane depending on voltage, being pulled

218 into the inner membrane leaflet by depolarization or pushed to the outer leaflet by

219 hyperpolarization. Thus, voltage steps can move DPA molecules closer to, or further from, the

220 donor by a fixed distance of 25 Å, reflecting to the estimated displacement of DPA[35,41]. These

221 qualities have been used to probe topography and conformational changes in several ion

222 channels from multiple groups[46-50]. We validated this approach using patch clamp fluorometry

223 where the fluorescence from single patch clamped cells, transfected with membrane tethered

224 CFP or YFP variants (mTurquiose2 and mVenus), was recorded in the continual presence of

225   DPA during a series of voltage steps (-180 mV to + 120 mV, 20 mV increments, Figure 1B).

226   Membrane tethered CFP (Lck-CFP) gave robust voltage-dependent fluorescence changes in

227   the presence of DPA (5 µM) but not in its absence ($\Delta F/F_{-15\ mv}$ = 0.45 ± 0.03, n = 6, Figure 1C &

228   D), consistent with the fluorophore being close to the plasma membrane and having a relatively

229   high R_0 distance (47 Å). The Lck-YFP gave relatively weak voltage-dependent quenching in the

230   presence of DPA ($\Delta F/F_{-15\ mv}$ = 0.16 ± 0.013, n = 6, Figure 1C & D), which is also consistent with

231   a membrane proximal position but relatively lower R_0 distance (36.5 Å).

232

233
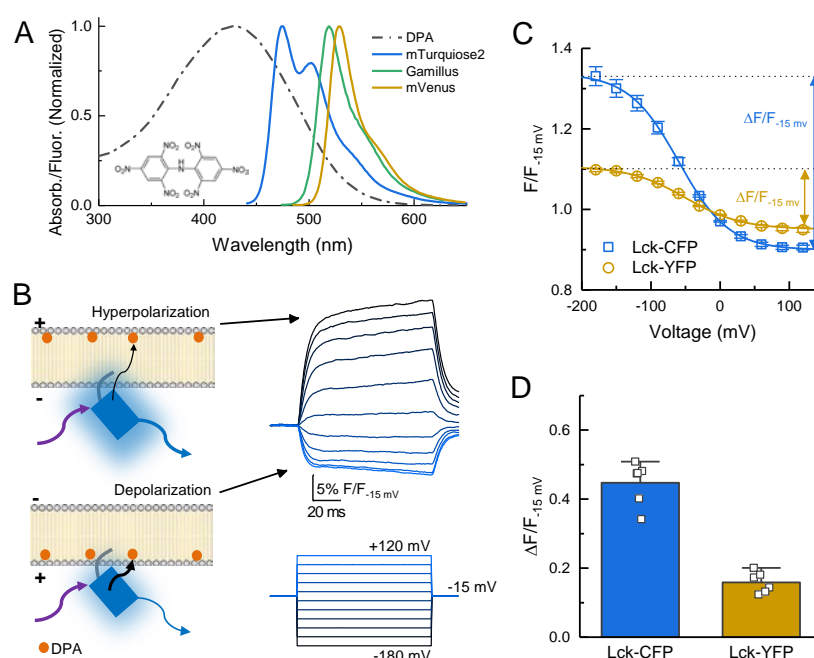
234   **Figure 1: Schematic of DPA quenching measurements. (A)** Absorption (*dotted line*) or fluorescence

235   emission (*solid lines*) spectra of DPA (*black*), CFP variant mTurqoise2 (*blue*), GFP variant Gamillus

236   (*green*) and YFP variant mVenus (*yellow*). Structure of DPA inset. **(B, *left*)** DPA (*orange circle*) localizes

237   to the outer leaflet with hyperpolarization and moves to inner leaflet upon depolarization, resulting in

238   stronger quenching. Arrows reflect excitation (*purple*), emission (*blue*) or resonance transfer (*black*). **(B,**

239   ***right*)** Exemplar patch fluorometry data of Lck-CFP fluorescence changing during voltage steps. **(C)**

240   Single cell fluorescence, normalized to fluorescence at -15 mV, over a range of voltages for Lck-CFP

241   (*blue*) and Lck-YFP (*yellow*). Solid lines are fits to Boltzmann function which yield $\Delta F/F$. **(D)** Summary of

242    $\Delta F/Fs$ from Lck-CFP or Lck-YFP. Squares are single cells (N = 6 cells per construct) and error bars depict

243   SEM.

244   Next, we set out to generate a coarse topographical map of chicken ASIC1 using DPA

245   quenching. To do this, we relied upon the steeply non-linear distance dependence of FRET. For

246   example, if DPA is close to a donor fluorophore then inducing a 25 Å displacement away using

247   voltage steps will produce a large change in fluorescence whereas if DPA is far from a donor

248   then a 25 Å displacement away will yield a much smaller effect (Supplemental Figure 1). We

249   inserted CFP or YFP immediately upstream of the N terminus and into four positions within the

250   C tail (Figure 2A, Supplemental Figure 2). The C tail positions were selected based on prior

251   divisions within this domain[17,18]. If the C tail is roughly parallel to the plasma membrane, as

252   observed for AMPA receptors[35], then all insertions will have equal voltage-dependent

253   quenching. However, if quenching varies at different insertion points and between fluorophores,

254   these data will provide insight into the topography of the tail. Importantly, fluorescent protein (FP)

255   insertions did not disrupt channel function as determined by the rates of desensitization and

256   recovery, although small differences in desensitization decay of C4 and recovery of C1 insertions

257   appeared (Supplemental Figure 3). Further, these constructs showed robust plasma membrane

258   localization in confocal microscopy (Supplemental Figure 4). For each construct, we measured

259   the fluorescence emission from single voltage clamped cells over a range of voltage steps before

260   DPA application, during continual application of 5 µM DPA and during a subsequent wash

261   period. Figure 2 shows the results of these experiments with extracellular pH 8 to maximally

262   populate the resting state. Importantly, the extent of quenching varied by position, ruling out the

263   possibility that the C tail is parallel to the membrane. Specifically, we found that with CFP

264   insertions, the C1 position gave the strongest quenching ($\Delta F/F_{-15\,mv} = 0.65 \pm 0.03$) with N and

265   C2 being about equal ($\Delta F/F_{-15\,mv} = 0.48 \pm 0.03$ and $\Delta F/F_{-15\,mv} = 0.51 \pm 0.05$) and C3 and C4

266   having progressively less quenching ($\Delta F/F_{-15\,mv} = 0.39 \pm 0.03$ and $\Delta F/F_{-15\,mv} = 0.21 \pm 0.03$). In

267   the case of YFP, a slightly different pattern was observed where the N terminal YFP gave the

268   strongest quenching ($\Delta F/F_{-15\,mv} = 0.26 \pm 0.02$) with C1-C4 giving progressively weaker quenching

269   ($\Delta F/F_{-15\,mv}$ between 0.23 ± 0.02 and 0.14 ± 0.01, Figure 2B-D).

270
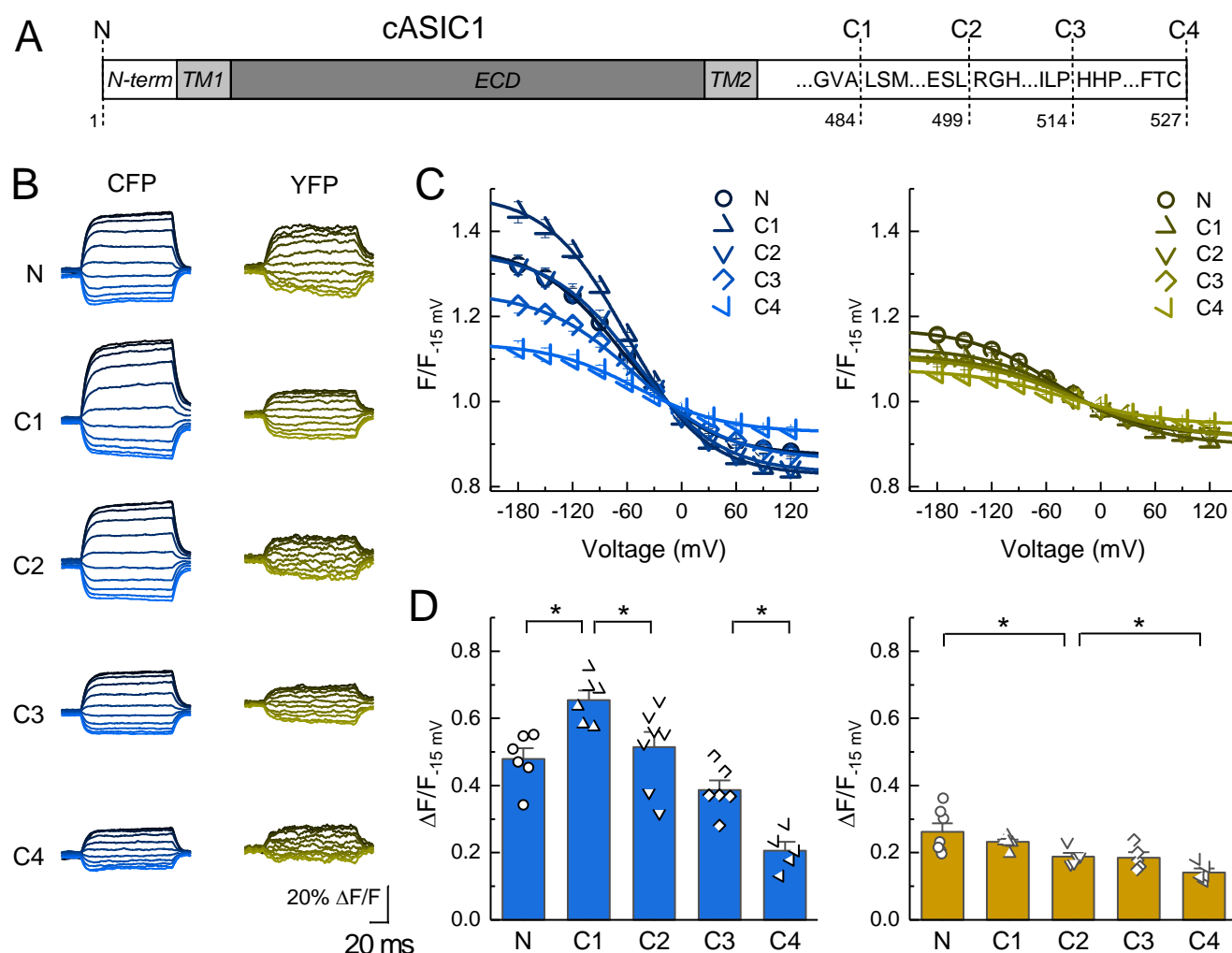
Figure 2: DPA quenching of CFP or YFP insertions in cASIC1 intracellular domains. (A) Schematic of cASIC1 constructs used. The extracellular domain (*ECD*) and transmembrane helices (*TM*) are grey with amino and carboxy termini depicted in white. Letters within the carboxy tail indicate the amino acid sequence around the insertion site while the lower numbers give the position. **(B)** Example fluorescence traces for each of the CFP or YFP insertions. Voltage protocol and coloring is the same as in Figure 1B. **(C & D)** Quenching curves and summary plots for CFP (*left*) and YFP (*right*) insertions. Symbols denote individual cells (N = 6 - 7 cells) and error bars represent SEM. Asterisks mark significant differences with p values of 0.00095 (N-C1), 0.024 (C1-C2), 0.00528 (C3-C4) for CFP and 0.038 (N-C2), 0.029 (C2-C4) for YFP.

271   To gain further insight from these data, we modelled DPA quenching of CFP and YFP

272   using previously established theory[35,41] (Supplemental Figure 5). The expected quenching of

273   CFP and YFP was simulated at infinitely negative and positive voltages over a range of distances

274   from the plasma membrane (Supplemental Figure 5A and B). Subtracting these curves and

275   normalizing produces the theoretical $\Delta F/F_{norm}$ curves as a function of distance for both CFP and

276   YFP (Supplemental Figure 5C). The CFP curve has a distinct hump at 24 Å (ie. 20 and 28 Å

277   give equal extents of quenching) while the YFP curve peaks at 16 Å and falls off with increasing

278   distance (Supplemental Figure 5C). This broadly mirrors the quenching pattern we observe in

279   our data with CFP C1 giving the greatest quenching followed by N and C2 then C3 and C4 while

280   in YFP all positions are weaker than N (Supplemental Figure 5C). The most parsimonious

281   interpretation of these data is that the N terminal insertion point is membrane proximal while all

282   positions in the C tail are progressively further from the membrane. To assign some provisional

283   distances to these measurements, we assumed the FP adds 10 angstroms to the axial distance,

284   reflecting the radius of the beta barrel. With this assumption, the strongest interpretation of our

285   data is that the tip of the N terminus is about 6-10 angstroms from the inner leaflet while the C1

286   insertion site is approximately 12-16 angstroms away. Distance estimates for the C2-C4

287   insertion sites are difficult to assign however given that the C4 position shows quenching for

288   both FPs, this final C terminal amino acids are likely within 30 to 40 angstroms of the inner leaflet.

289   For reference, the C-α to C-α distance from the critical His74 to Lys355, at the base of thumb

290   domain's alpha5 helix, is 35 angstroms (resting state, PDB:6VTL). Uncertainties and caveats to

291   these estimates are enumerated in the Discussion section. Increases in accuracy to this

292   provisional map will require reductions in background fluorescence and a smaller fluorophore at

293   more positions.

294   *N and C tail inter versus intra subunit interactions*

295   The DPA quenching experiments indicate the N terminal insertion is closest to the plasma

296   membrane, while the C1-C4 insertions are progressively further away. Within the membrane

297   proximal segment of the C tail is a cluster of lysine and arginine residues (amino acids 461 –

298   476). These have been proposed to interact with a segment of negatively charged amino acids

299   in the N termini (amino acids 7-12), forming a salt bridge between the intracellular tails of the

300   same subunit[17,18]. We reasoned that if such a bridge was formed between tails of the same

301   subunit, then FPs appended to both tails of the same subunit would experience stronger FRET

302   than FPs on the tails of different subunits. To test this, we used fluorescent lifetime imaging

303   (FLIM) to measure the lifetime of an N terminal CFP donor in the absence or presence of a C

304   terminal YFP acceptor. A challenge in this experiment is ensuring that only one FRET pair exists

305   within the majority of trimers. If more than one pair of FPs are present, a 'donor-centric' measure

306   of FRET like FLIM will be skewed towards higher FRET efficiencies[51]. To measure the FRET

307   between CFP and YFP in a single subunit we appended a C terminal YFP to the N terminal CFP

308   clone (CFP-cA1-YFP, Supplemental Figure 2). This construct was transfected along with wild

309   type cASIC1 at progressively increasing ratios. In principle, as the amount of unlabeled wild type

310   cASIC1 increases, the FRET should decrease (lifetimes increase) until a plateau is reached.

311   The FRET value of this plateau will correspond to the FRET from single subunits. As expected,

312   CFP-cA1-YFP alone produced very strong FRET as evidenced by the dramatically faster CFP

313   lifetimes compared to N CFP (N CFP: 4.06 ± 0.02 ns, n = 76; CFP-cA1-YFP: 2.68 ± 0.03, n =

314   58, Figure 3). Adding more wild type cASIC1 led to an increase in CFP lifetimes until reaching a

315   plateau of approximately 3 ns, representing a FRET efficiency of 25% between CFP and YFP in

316   a single subunit (1:31 ratio: 3.08 ± 0.03, n = 34, 24% FRET efficiency, Figure 3C).
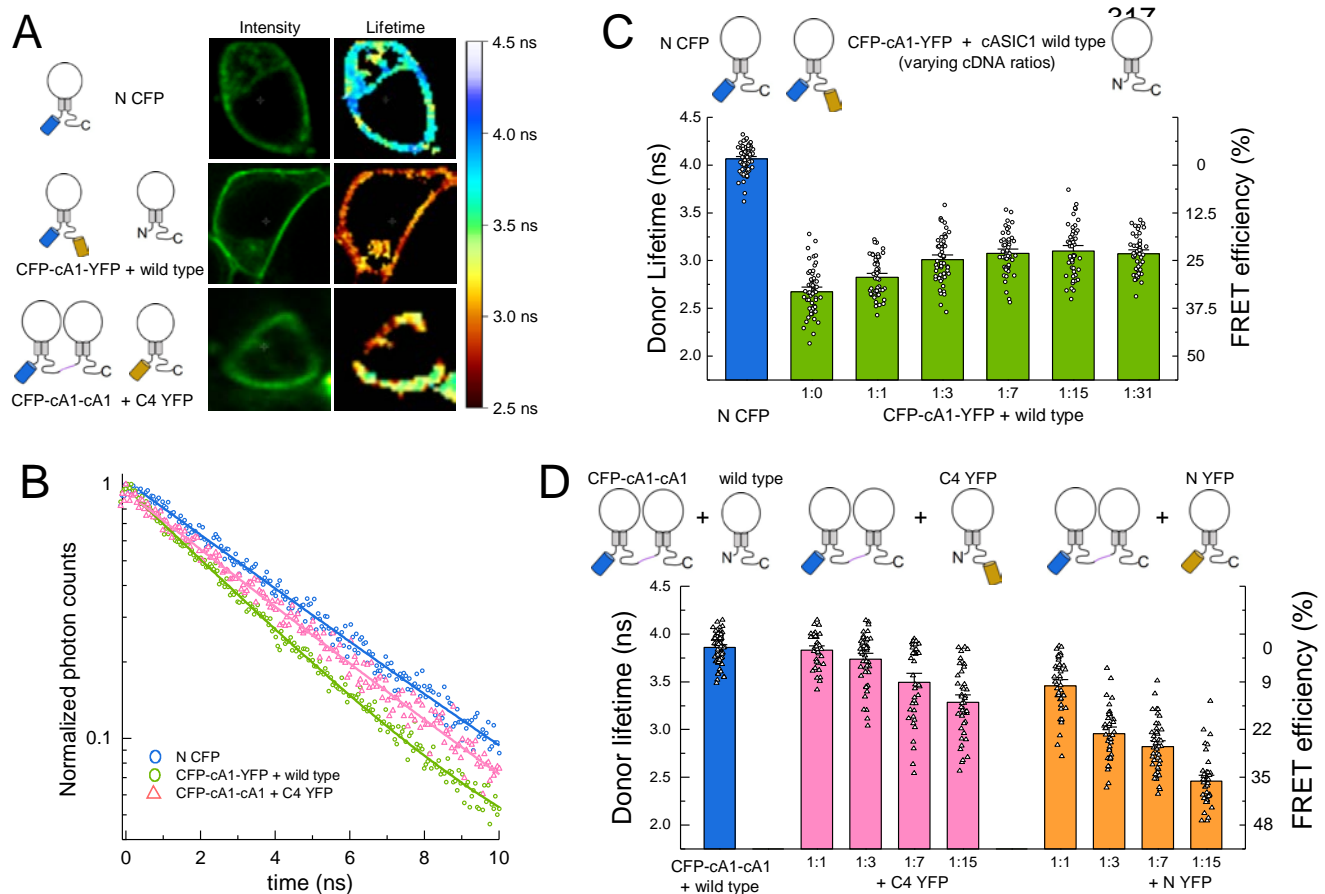
Figure 3: FRET is stronger within subunits than between subunits (A) Example cells transfected with the indicated constructs showing intensity (*left*) and lifetime (*right*) images. **(B)** TCSPC histograms from the plasma membrane of cells in A and additional control. Solid line is a single exponential fit to the data. **(C)** Cartoon (*upper*) and lifetimes (*lower*) from the indicated constructs for measuring intra-subunit FRET. **(D)** Cartoon (*upper*) and lifetimes (*lower*) for measuring inter subunit FRET. Symbols denote single cells (N = 35 – 76 cells) and error bars are SEM.

318   To measure the FRET between FPs in different subunits, we concatenated two cASIC1

319 subunits together in a dimer with an N terminal CFP (CFP-cA1-cA1, Supplemental Figure 2).

320 Expression of this clone along with wild type cASIC1 gave the expected ~ 4 ns mono-exponential

321 lifetime from this CFP variant (3.86 ± 0.02 ns, n = 74). Co-transfection of CFP-cA1-cA1 along

322 with C4 YFP at increasing ratios produced progressively faster lifetimes up to about 3.3 ns or

323 15% FRET efficiency (1:15: 3.28 ± 0.05 ns, n = 43, Figure 3). In this experiment, FRET comes

324 partly from the CFP-cA1-cA1 transferring energy to a YFP within the channel complex and partly

325   from transfer to YFPs in nearby ASICs (ie. crowding). This crowding effect is illustrated in

326   Supplemental Figure 6 where CFP-cA1-cA1 is co-expressed with unlabeled wild type and Lck-

327   YFP at varying ratios. As the Lck-YFP amount is increased so does the FRET efficiency.

328   Separating out the fraction of FRET due to crowding is difficult but also unnecessary in this case.

329   Even with a 1:15 ratio of CFP-cA1-cA1 to C4 YFP, where all dimers likely have a C4 YFP

330   monomer partner, the FRET efficiency is significantly less than that observed in the CFP-cA1-

331   YFP experiment (15 ± 1%, n = 43 for CFP-cA1-cA1 + C4 YFP 1:15; 24 ± 1%, n = 46 for CFP-

332   cA1-YFP + wild type 1:15, p < 1e-6, student's t-test). Thus, FPs on the same subunit show more

333   efficient FRET than on different subunits, suggesting the tails of the same subunit are physically

334   closer and more likely to associate.

335   The addition of C4 YFP at 1:1 and 1:3 ratios gave unexpectedly small FRET efficiencies

336   (1 ± 1% and 3 ± 1%, n = 35 and 46). To determine if the concatenated dimer was assembling

337   as anticipated, we repeated the experiment using N YFP, where the acceptor is positioned much

338   closer to the donor and hence should give more robust FRET. Consistent with this, all ratios of

339   N YFP gave a strong reduction in donor lifetimes, indicating the CFP dimer does assemble with

340   labelled monomer. Taken together, these experiments demonstrate that FRET efficiency from

341   FPs on neighboring subunits is considerably less than that measured from the same subunit,

342   supporting a model where the N and C tails of the same subunit interact.

343   *Measurement of intracellular domain conformational changes*

344   The putative salt bridge between the N terminal tail and the membrane proximal segment

345   of the C tail is proposed to break apart to facilitate ion-independent signaling[17]. Evidence for this

346   movement comes from the change in FRET between N terminal CFP and C terminal YFP upon

347   extracellular acidification[17]. To investigate this, we conducted an analogous experiment using

348 patch clamp fluorometry with simultaneous recording of both the blue and yellow emission from

349 CFP-cA1-YFP receptors. As seen in Figure 4A and B, rapid application of pH 7 or 6, but not pH

350 8, produced a decrease in the ratio of YFP to CFP emission (ie. apparent FRET) with a slow

351 time course ($\Delta FRET_{app}$ pH 7: -2.6 ± 0.3%, n = 8, p = 0.006 versus pH 8; pH 6: -4.6 ± 0.5%, n =

352 8, p = 0.0004 versus pH 8). However, as discussed previously[17], the strong pH sensitivity of YFP

353 complicates the interpretation of these measurements. Consistent with this[17], we also observed

354 a strong loss of emission from C4 YFP upon extracellular acidification (Figure 4A and B, ΔF_{norm}

355 pH 7: -2.6 ± 0.8%, n = 5; pH 6: -12 ± 2%, n = 8). In contrast, the N CFP showed no such change

356 in emission (Figure 4) owing to this CFP variants pKa of 3.1[40].

357 Blue/yellow and green/red pairings are the most common for FRET. The chromophore of

358 GFP is intrinsically pH sensitive and because YFP is a derivative of GFP, pH sensitivity will

359 always be a concern for these FPs. Fortunately, a novel GFP was described with a distinct

360 chromophore and pKa of 3.4[52]. When combined with a relatively low pKa red fluorescent protein

361 (TagRFP, pKa 3.8[53]), this pairing should enable a FRET measurement that is relatively

362 insensitive to the pH range examined while gaining the advantages of green/red FRET[39]. We

363 therefore cloned the low pKa GFP into the N terminal position and the RFP into the C4 position

364 (GFP-cA1 and cA1-RFP, Supplemental Figure 2) and tested the pH sensitivity of their

365 fluorescence emission. As seen in Figure 4C and D, both clones showed no change in their

366 fluorescence emission with extracellular pH 6, 7 or 8, confirming their suitability for measuring

367 conformational changes induced by pH. We next added both FPs into a single subunit (GFP-

368 cA1-RFP) and repeated our dual channel patch clamp fluorometry measurements. However, we

369 detected no change in apparent FRET between these FPs (Figure 4C and D, numbers).

370 Importantly, the GFP does FRET with the RFP as the ratio of red to green fluorescence emission

371 was significantly greater in the GFP-cA1-RFP clone compared to the GFP-cA1 only (GFP-cA1:

372 0.14 ± 0.01, n = 6; GFP-cA1-RFP: 0.41 ± 0.04, n = 7, p = 0.0007). To increase the sensitivity to

373 local motions, we repeated the experiment with the RFP cloned into the C1 position (ie. GFP-

374 cA1-C1-RFP). Unfortunately, here again we did not detect any change in apparent FRET with

375 either GFP-cA1-C1-RFP alone or when diluting this construct out with unlabeled wild type

376 cASIC1 ($\Delta FRET_{app}$ GFP-cA1-C1-RFP pH 6: -0.9 ± 1.4%, n = 3; + wild type pH 6: -0.8 ± 1.5%, n

377 = 5; Supplemental Figure 7). Although we did not detect any changes in FRET, we cannot

378 exclude that extracellular acidification does cause the N and C tails do move apart laterally but

379 such movements are either small, localized or otherwise fall below our ability to detect them.
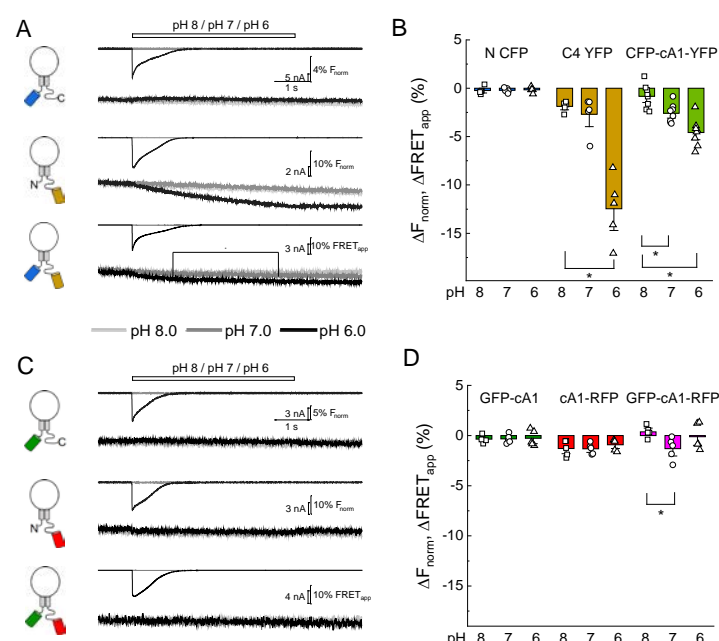
Figure 4: Extracellular acidification produces no change in FRET when using pH-insensitive FPs.
(A) Cartoons (*left*), electrophysiology (*upper*) and fluorescence traces (*lower*) from single cells transfected with the CFP, YFP or both FPs attached to cASIC1 during pH jumps from 8 into pH 8, pH 7 or pH 6. Fluorescence trace is the acceptor fluorescence signal divided by the donor. **(B)** Summary of change in acceptor/donor ratio during pH changes. **(C)** Same as in A but for pH-insensitive variants of GFP and RFP (see Methods). **(D)** Summary of change in acceptor/donor ratio during pH changes. Symbols indicate single cells (N = 5 - 8 cells), error bars are SEM.

380   Finally, we investigated if either the N or C tails move axially, with respect to the plasma

381   membrane, upon extracellular acidification. To do this, we returned to DPA quenching by first

382   recording the fluorescence emission during a series of voltage steps in the absence of DPA,

383   presence of DPA at pH 8.0 and then in the presence of DPA at pH 6.0. Importantly, the voltage

384   dependent quenching of Lck-CFP was not different between extracellular pH 8 compared to pH

385   6 ($\Delta F/F_{-15\,mV}$ pH 8: 0.45 ± 0.03, pH 6: 0.43 ± 0.04, n = 6, p = 0.52, paired t-test, Figure 5), thus

386   confirming the DPA quenching is relatively pH-tolerant. Interestingly, the extent of quenching at

387   the N and C1 position was significantly reduced in pH 6 compared to pH 8 (Figure 5). Specifically,

388   in the resting state (pH 8), CFP at the N or C1 position had a $\Delta F/F_{-15\,mV}$ of 0.49 ± 0.02 or 0.57 ±

389   0.04 (n = 13 or 11), respectively. However, with extracellular pH 6 (populating the desensitized

390   state), these were reduced to 0.41 ± 0.02 and 0.55 ± 0.03. In a subset of cells expressing the N

391   CFP clone, we maintained the recording in pH 8, 6 and then back to pH 8 and found the effect

392   on the extent of quenching was readily reversible (Supplemental Figure 8). None of the other

393   positions showed significant evidence of movement between these conditions (Figure 4B-C),

394   supporting that this motion is specific to the membrane proximal region and not a general pH

395   artefact. These results demonstrate that both the N and C tails of cASIC1 moves axially with

396   respect to the membrane between the resting and desensitized states. To determine if the axial

397   motion is toward or away from the plasma membrane, we considered our prior data and

398   theoretical analysis (Figure 2, Supplemental Figure 5). The resting state DPA quenching place

399   the N terminal FP chromophore about 15-20 angstroms from the inner membrane leaflet (Figure

400   2, Supplemental Figure 5). The reduced quenching in the pH 6 condition indicates the FP moves

401   even closer to the plasma membrane upon channel desensitization. However, interpreting the

402   C1 data is less straightforward. The DPA data indicate FPs at the C1 position are about 23-25

403 angstroms from the inner leaflet, thus lying at or near the peak of CFP's $\Delta F/F_{norm}$ curve

404 (Supplemental Figure 5C and D). In such a position, moving either towards or away from the

405 plasma membrane will result in decreased quenching. A scenario where the N terminal moves

406 towards the membrane while the C tail moves away is difficult to reconcile with the lack of ΔFRET

407 between FPs in these positions upon acidification (Figure 4). Therefore, our data favor a model

408 where the N and proximal segment of the C tail move up towards the inner membrane leaflet

409 when the channel is exposed to desensitizing conditions (Figure 6).
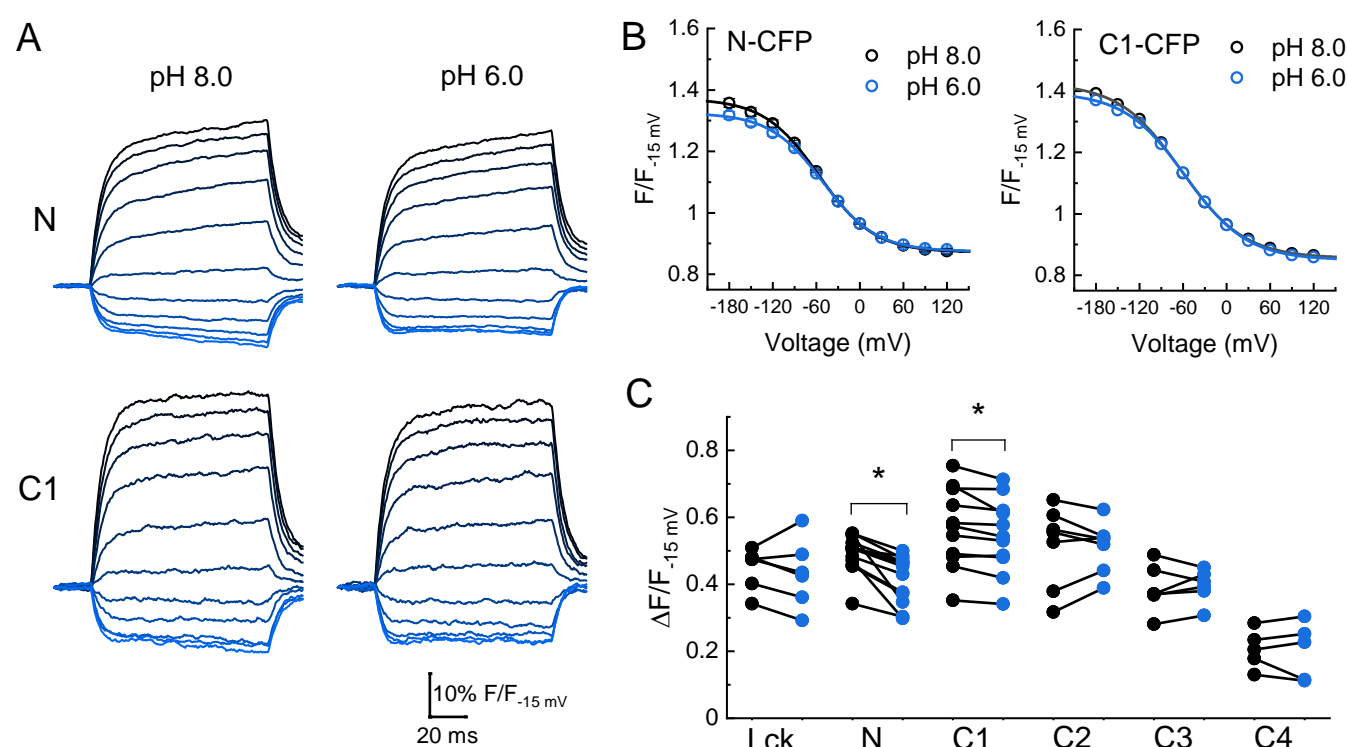
Figure 5: Desensitization induces an axial motion of the membrane proximal region. (A) Example CFP fluorescence quenching traces from single cells expressing N or C1 CFP-cASIC1 with extracellular pH 8 (*left*) or pH 6 (*right*). **(B)** Quenching voltage curves for CFP inserted in N (*left*) or C1 (*right*) position. Curves in extracellular pH 8.0 (resting state) shown in black and pH 6.0 (desensitized) in blue. **(C)** Summary of the extents of quenching at each position with extracellular pH 8 (*black*) and 6 (*blue*). Symbols denote individual cells (N = 5 – 13 cells per construct) and error bars represent SEM. * indicates p value < 0.05 by Wilcoxon rank sum test.

410

411
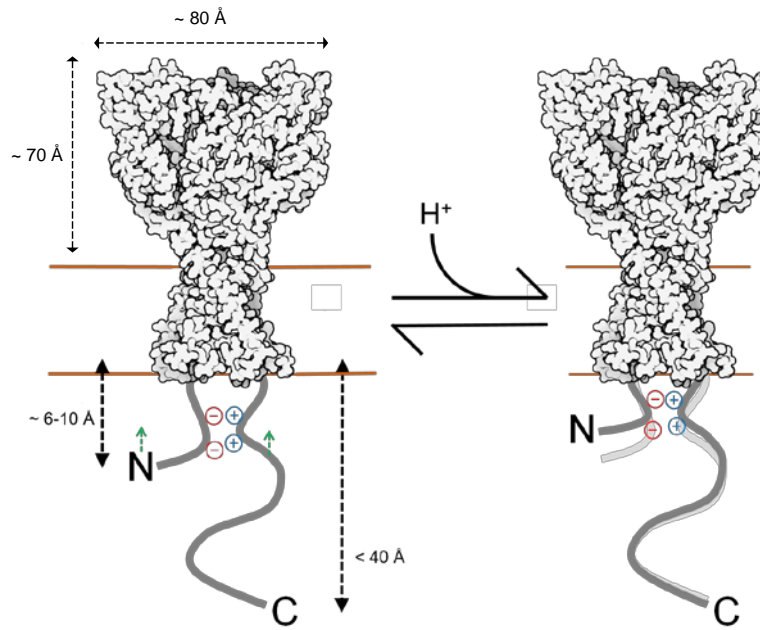
Figure 6: Cartoon of topography and acid-inducted motions for cASIC1. Estimated distances of N and C tail positions derived from DPA quenching mapped onto resting state structure (6VTL). Not drawn to scale. Extracellular pH moves the proximal N and C segments towards the membrane.

Discussion and Conclusion

Using a combination of patch clamp fluorometry and FLIM, we obtained an outline of the ASIC intracellular domains. We find the N terminus and proximal segment of the C terminus to extend about 6-10 and 12-16 angstroms into the cytosol, while the remainder of the C tail projects not more than 40 angstroms. Further, FLIM FRET results indicate the N and proximal segment of the C tail from the same subunit are physically closer than from different subunits, presumably reflecting association via the putative salt bridge. Finally, we find that the N and proximal segment of the C tail move towards the plasma membrane upon acidification, while we detect no substantial lateral movement (Figure 6). Our results support the emerging idea that extracellular acidification promotes ASIC ICD conformational changes, potentially creating or exposing sites within the membrane proximal segments that bind intracellular signaling partners and facilitating metabotropic signaling.

Sources of error

The principle source of error is the possible disruption of the N or C tail caused by the addition or insertion of a fluorescent protein. Future studies could employ smaller fluorophores such as the fluorescent non-canonical amino acid L-ANAP[54-56] or split inteins and semi synthesis[57-59] to introduce small, bright fluorophores in specific sites. Such methods, ideally combined with acceptor groups[54-56], will refine and test the provisional map we report here. An additional source of error in our DPA quenching estimates is the background fluorescence from FPs in the ER. These FPs may be either unquenched or progressively quenched over the course of the experiment as DPA migrates into the cell. In prior work, intracellular channels and FPs produced variable amounts of background fluorescence[35,48,50], which may confound more accurate mapping. Fortunately, our family of cASIC1 with FP insertions show very robust plasma

435 membrane expression (Supplemental Figure 4). We also selected cells with minimal intracellular

436 fluorescence to reduce the impact of this background signal. A further source of potential error

437 is the orientation dependence of FRET. This concern is partly mitigated since the fluorophores

438 is attached to regions which are likely to be unstructured or highly flexible, allowing the FPs to

439 adopt multiple orientations. Consistent with this, past theoretical and experimental work

440 suggests a minimal influence of orientation dependence for FRET involving DPA as an

441 acceptor[35]. Subsequent studies using isotropic resonance transfer methods such as tmFRET or

442 LRET may reduce many of these concerns and provide a more refined map.

443 *Structural interpretation*

444 Structures of full-length cASIC1 have been solved using cryo-EM. The N and C tails are present

445 in these constructs yet give no resolvable density[24,25]. This suggests the tails maybe largely

446 disordered, waiting to bind intracellular proteins via an induced fit or conformation selection

447 mechanisms[60,61]. If true, then our data define the borders of the conformation landscape these

448 disordered segments occupy. However, it is also possible that within these disordered tails are

449 areas of secondary structure. A small but well-ordered segment of the tails which is moved

450 around by adjacent disordered regions might be unresolvable by cryo-EM. Having isolated

451 regions of order amongst a largely disordered tail is consistent with the proposed salt bridge

452 between N and the C1 region. Secondary structure predictions also support this view, with the

453 proximal segment of the C tail having a strong tendency to form alpha helices while the

454 remainder of the tail is unstructured. Additional approaches such as CD spectroscopy combined

455 with molecular modelling[62], NMR and DEER will be critical to address the extent and location of

456 secondary structure within the tails as well as further define the intracellular structural changes

457 induced by extracellular pH that we report here. A particularly useful approach maybe smFRET,

458   which has already been used to gain insight into the unstructured, and larger, intracellular tails

459   of NMDA receptors[63,64].

460   *Physiological relevance*

461   Numerous protein-protein interactions have been reported for ASICs that are important for

462   channel trafficking, gating, and possibly metabotropic signaling[34,65]. The best documented of

463   these are PICK1, PSD-95 and stomatin[29-31,33,66-68]. Of particular note, is the interaction between

464   ASIC3's C tail and stomatin, which enables stomatin to inhibit channel activation through a

465   mechanism involving the first transmembrane helix[31]. In addition, recent work has suggested

466   that the membrane proximal region of the ASIC1 C tail becomes liberated from the N-tail during

467   desensitization, allowing for the recruitment of RIP1 kinase[17]. This results in activation of RIP1

468   by phosphorylation leading to eventual cell death via necroptosis. Canonical activation of RIP1

469   by the tumor necrosis factor (TNF) receptor 1 (TNFR1) occurs through heterodimerization of

470   death domains (DD) present on both RIP1 and TNFR1[69]. ASIC1 does not contain a death

471   domain, so how RIP1 interacts with the C-tail of ASIC1 and resulting in activation remains an

472   important unanswered question. Using the FP insertion approach we adopted is problematic for

473   investigating this, or any of the other protein-protein interactions mentioned above, due to the

474   sheer disruptive size of the FP. However, using a higher resolution method with a smaller

475   fluorophore could shed light on the molecular determinants, timing and dynamics of these

476   interactions. Thus the future of investigating the ASIC ICDs will be bright.

References

477

478   1   Pattison, L. A., Callejo, G. & St John Smith, E. Evolution of acid nociception: ion channels and
479   receptors for detecting acid. *Philosophical transactions of the Royal Society of London. Series*
480   *B, Biological sciences* **374**, 20190291, doi:10.1098/rstb.2019.0291 (2019).
481   2   Du, J. *et al.* Protons are a neurotransmitter that regulates synaptic plasticity in the lateral
482   amygdala. *Proc Natl Acad Sci U S A* **111**, 8961-8966, doi:10.1073/pnas.1407018111 (2014).
483   3   Kreple, C. J. *et al.* Acid-sensing ion channels contribute to synaptic transmission and inhibit
484   cocaine-evoked plasticity. *Nat Neurosci* **17**, 1083-1091, doi:10.1038/nn.3750 (2014).
485   4   Yu, Z. *et al.* The acid-sensing ion channel ASIC1a mediates striatal synapse remodeling and
486   procedural motor learning. *Sci Signal* **11**, doi:10.1126/scisignal.aar4481 (2018).
487   5   Liu, M. G. *et al.* Acid-sensing ion channel 1a contributes to hippocampal LTP inducibility through
488   multiple mechanisms. *Scientific reports* **6**, 23350, doi:10.1038/srep23350 (2016).
489   6   Uchitel, O. D., Gonzalez Inchauspe, C. & Weissmann, C. Synaptic signals mediated by protons
490   and acid-sensing ion channels. *Synapse* **73**, e22120, doi:10.1002/syn.22120 (2019).
491   7   Du, J. *et al.* Transient acidosis while retrieving a fear-related memory enhances its lability. *Elife*
492   **6**, doi:10.7554/eLife.22564 (2017).
493   8   Taugher, R. J. *et al.* The amygdala differentially regulates defensive behaviors evoked by CO2.
494   *Behav Brain Res* **377**, 112236, doi:10.1016/j.bbr.2019.112236 (2020).
495   9   Taugher, R. J. *et al.* ASIC1A in neurons is critical for fear-related behaviors. *Genes Brain Behav*
496   **16**, 745-755, doi:10.1111/gbb.12398 (2017).
497   10   Taugher, R. J. *et al.* The bed nucleus of the stria terminalis is critical for anxiety-related behavior
498   evoked by CO2 and acidosis. *J Neurosci* **34**, 10247-10255, doi:10.1523/JNEUROSCI.1680-
499   14.2014 (2014).
500   11   Ziemann, A. E. *et al.* Seizure termination by acidosis depends on ASIC1a. *Nat Neurosci* **11**,
501   816-822, doi:10.1038/nn.2132 (2008).
502   12   Xiong, Z. G. *et al.* Neuroprotection in ischemia: blocking calcium-permeable acid-sensing ion
503   channels. *Cell* **118**, 687-698, doi:10.1016/j.cell.2004.08.026 (2004).
504   13   Wemmie, J. A., Taugher, R. J. & Kreple, C. J. Acid-sensing ion channels in pain and disease.
505   *Nat Rev Neurosci* **14**, 461-471, doi:10.1038/nrn3529 (2013).
506   14   Grunder, S. & Pusch, M. Biophysical properties of acid-sensing ion channels (ASICs).
507   *Neuropharmacology* **94**, 9-18, doi:10.1016/j.neuropharm.2014.12.016 (2015).
508   15   Benson, C. J. *et al.* Heteromultimers of DEG/ENaC subunits form H+-gated channels in mouse
509   sensory neurons. *Proc Natl Acad Sci U S A* **99**, 2338-2343, doi:10.1073/pnas.032678399
510   (2002).
511   16   Ruan, Z., Osei-Owusu, J., Du, J., Qiu, Z. & Lu, W. Structures and pH-sensing mechanism of the
512   proton-activated chloride channel. *Nature* **588**, 350-354, doi:10.1038/s41586-020-2875-7
513   (2020).
514   17   Wang, J. J. *et al.* Disruption of auto-inhibition underlies conformational signaling of ASIC1a to
515   induce neuronal necroptosis. *Nature communications* **11**, 475, doi:10.1038/s41467-019-13873-0
516   (2020).
517   18   Wang, Y.-Z. *et al.* Tissue acidosis induces neuronal necroptosis via ASIC1a channel
518   independent of its ionic conduction. *eLife* **4**, e05682, doi:10.7554/eLife.05682 (2015).
519   19   Rodriguez-Moreno, A. & Sihra, T. S. Kainate receptors with a metabotropic modus operandi.
520   *Trends Neurosci* **30**, 630-637, doi:10.1016/j.tins.2007.10.001 (2007).
521   20   Dore, K. *et al.* Unconventional NMDA Receptor Signaling. *J Neurosci* **37**, 10800-10807,
522   doi:10.1523/JNEUROSCI.1825-17.2017 (2017).
523   21   Kabbani, N. & Nichols, R. A. Beyond the Channel: Metabotropic Signaling by Nicotinic
524   Receptors. *Trends Pharmacol Sci* **39**, 354-366, doi:10.1016/j.tips.2018.01.002 (2018).
525   22   Valbuena, S. & Lerma, J. Non-canonical Signaling, the Hidden Life of Ligand-Gated Ion
526   Channels. *Neuron* **92**, 316-329, doi:10.1016/j.neuron.2016.10.016 (2016).

23   Pressey, J. C. & Woodin, M. A. Kainate receptor regulation of synaptic inhibition in the hippocampus. *J Physiol* **599**, 485-492, doi:10.1113/JP279645 (2021).

24   Yoder, N. & Gouaux, E. The His-Gly motif of acid-sensing ion channels resides in a reentrant 'loop' implicated in gating and ion selectivity. *Elife* **9**, doi:10.7554/eLife.56527 (2020).

25   Yoder, N., Yoshioka, C. & Gouaux, E. Gating mechanisms of acid-sensing ion channels. *Nature* **555**, 397, doi:10.1038/nature25782 (2018).

26   Baconguis, I., Bohlen, C. J., Goehring, A., Julius, D. & Gouaux, E. X-ray structure of acid-sensing ion channel 1-snake toxin complex reveals open state of a Na(+)-selective channel. *Cell* **156**, 717-729, doi:10.1016/j.cell.2014.01.011 (2014).

27   Gonzales, E. B., Kawate, T. & Gouaux, E. Pore architecture and ion sites in acid-sensing ion channels and P2X receptors. *Nature* **460**, 599, doi:10.1038/nature08218 (2009).

28   Chai, S. *et al.* A kinase-anchoring protein 150 and calcineurin are involved in regulation of acid-sensing ion channels ASIC1a and ASIC2a. *J Biol Chem* **282**, 22668-22677, doi:10.1074/jbc.M703624200 (2007).

29   Baron, A. *et al.* Protein kinase C stimulates the acid-sensing ion channel ASIC2a via the PDZ domain-containing protein PICK1. *J Biol Chem* **277**, 50463-50468, doi:10.1074/jbc.M208848200 (2002).

30   Hruska-Hageman, A. M., Benson, C. J., Leonard, A. S., Price, M. P. & Welsh, M. J. PSD-95 and Lin-7b interact with acid-sensing ion channel-3 and have opposite effects on H+- gated current. *J Biol Chem* **279**, 46962-46968, doi:10.1074/jbc.M405874200 (2004).

31   Klipp, R. C., Cullinan, M. M. & Bankston, J. R. Insights into the molecular mechanisms underlying the inhibition of acid-sensing ion channel 3 gating by stomatin. *The Journal of general physiology* **152**, doi:10.1085/jgp.201912471 (2020).

32   Schnizler, M. K. *et al.* The cytoskeletal protein alpha-actinin regulates acid-sensing ion channel 1a through a C-terminal interaction. *J Biol Chem* **284**, 2697-2705, doi:10.1074/jbc.M805110200 (2009).

33   Leonard, A. S. *et al.* cAMP-dependent protein kinase phosphorylation of the acid-sensing ion channel-1 regulates its binding to the protein interacting with C-kinase-1. *Proc Natl Acad Sci U S A* **100**, 2029-2034, doi:10.1073/pnas.252782799 (2003).

34   Kellenberger, S. & Schild, L. International union of basic and clinical pharmacology. XCI. structure, function, and pharmacology of acid-sensing ion channels and the epithelial Na+ channel. *Pharmacological reviews* **67**, 1-35, doi:10.1124/pr.114.009225 (2015).

35   Zachariassen, L. G. *et al.* Structural rearrangement of the intracellular domains during AMPA receptor activation. *Proc Natl Acad Sci U S A* **113**, E3950-3959, doi:10.1073/pnas.1601747113 (2016).

36   Rook, M. L., Williamson, A., Lueck, J. D., Musgaard, M. & Maclean, D. M. beta11-12 linker isomerization governs Acid-sensing ion channel desensitization and recovery. *Elife* **9**, doi:10.7554/eLife.51111 (2020).

37   Rook, M. L. *et al.* Mutation of a conserved Gln residue does not abolish desensitization of acid-sensing ion channel 1. *bioRxiv*, 2020.2012.2019.423606, doi:10.1101/2020.12.19.423606 (2020).

38   MacLean, D. M. in *Ionotropic Glutamate Receptor Technologies* (ed G. K. Popescu) Ch. 12, 165-183 (Springer, 2015).

39   McCullock, T. W., MacLean, D. M. & Kammermeier, P. J. Comparing the performance of mScarlet-I, mRuby3, and mCherry as FRET acceptors for mNeonGreen. *PloS one* **15**, e0219886, doi:10.1371/journal.pone.0219886 (2020).

40   Goedhart, J. *et al.* Structure-guided evolution of cyan fluorescent proteins towards a quantum yield of 93%. *Nature communications* **3**, 751, doi:10.1038/ncomms1738 (2012).

41   Wang, D., Zhang, Z., Chanda, B. & Jackson, M. B. Improved probes for hybrid voltage sensor imaging. *Biophysical journal* **99**, 2355-2365, doi:10.1016/j.bpj.2010.07.037 (2010).

577 42 Lambert, T. J. FPbase: a community-editable fluorescent protein database. *Nature methods* **16**, 277-278, doi:10.1038/s41592-019-0352-8 (2019).

579 43 Gunupuru, R., Kesharwani, M. K., Chakraborty, A., Ganguly, B. & Paul, P. Dipicrylamine as a colorimetric sensor for anions: experimental and computational study. *RSC Adv.* **4**, 53273-53281, doi:10.1039/c4ra09099c (2014).

582 44 Miller, W. G. & Goebel, C. V. Dimensions of protein random coils. *Biochemistry* **7**, 3925-3935, doi:10.1021/bi00851a021 (1968).

584 45 Chanda, B. *et al.* A hybrid approach to measuring electrical activity in genetically specified neurons. *Nat Neurosci* **8**, 1619-1626, doi:10.1038/nn1558 (2005).

586 46 Chanda, B., Asamoah, O. K., Blunck, R., Roux, B. & Bezanilla, F. Gating charge displacement in voltage-gated ion channels involves limited transmembrane movement. *Nature* **436**, 852-856, doi:10.1038/nature03888 (2005).

589 47 Groulx, N., Juteau, M. & Blunck, R. Rapid topology probing using fluorescence spectroscopy in planar lipid bilayer: the pore-forming mechanism of the toxin Cry1Aa of Bacillus thuringiensis. *The Journal of general physiology* **136**, 497-513, doi:10.1085/jgp.200910347 (2010).

592 48 Barros, F., Dominguez, P. & de la Pena, P. Relative positioning of Kv11.1 (hERG) K(+) channel cytoplasmic domain-located fluorescent tags toward the plasma membrane. *Scientific reports* **8**, 15494, doi:10.1038/s41598-018-33492-x (2018).

595 49 Taraska, J. W. & Zagotta, W. N. Structural dynamics in the gating ring of cyclic nucleotide-gated ion channels. *Nature structural & molecular biology* **14**, 854-860, doi:10.1038/nsmb1281 (2007).

597 50 De-la-Rosa, V., Rangel-Yescas, G. E., Ladron-de-Guevara, E., Rosenbaum, T. & Islas, L. D. Coarse architecture of the transient receptor potential vanilloid 1 (TRPV1) ion channel determined by fluorescence resonance energy transfer. *J Biol Chem* **288**, 29506-29517, doi:10.1074/jbc.M113.479618 (2013).

601 51 Ben-Johny, M., Yue, D. N. & Yue, D. T. Detecting stoichiometry of macromolecular complexes in live cells using FRET. *Nature communications* **7**, 13709, doi:10.1038/ncomms13709 (2016).

603 52 Shinoda, H. *et al.* Acid-Tolerant Monomeric GFP from Olindias formosa. *Cell Chem Biol* **25**, 330-338 e337, doi:10.1016/j.chembiol.2017.12.005 (2018).

605 53 Merzlyak, E. M. *et al.* Bright monomeric red fluorescent protein with an extended fluorescence lifetime. *Nature methods* **4**, 555-557, doi:10.1038/nmeth1062 (2007).

607 54 Zagotta, W. N., Gordon, M. T., Senning, E. N., Munari, M. A. & Gordon, S. E. Measuring distances between TRPV1 and the plasma membrane using a noncanonical amino acid and transition metal ion FRET. *The Journal of general physiology* **147**, 201-216, doi:10.1085/jgp.201511531 (2016).

611 55 Gordon, S. E., Senning, E. N., Aman, T. K. & Zagotta, W. N. Transition metal ion FRET to measure short-range distances at the intracellular surface of the plasma membrane. *The Journal of general physiology* **147**, 189-200, doi:10.1085/jgp.201511530 (2016).

614 56 Gordon, S. E., Munari, M. & Zagotta, W. N. Visualizing conformational dynamics of proteins in solution and at the cell membrane. *Elife* **7**, doi:10.7554/eLife.37248 (2018).

616 57 Khoo, K. K. *et al.* Chemical modification of proteins by insertion of synthetic peptides using tandem protein trans-splicing. *Nature communications* **11**, 2284, doi:10.1038/s41467-020-16208-6 (2020).

619 58 Lueck, J. D. *et al.* Atomic mutagenesis in ion channels with engineered stoichiometry. *Elife* **5**, doi:10.7554/eLife.18976 (2016).

621 59 Shah, N. H. & Muir, T. W. Inteins: Nature's Gift to Protein Chemists. *Chemical science* **5**, 446-461, doi:10.1039/c3sc52951g (2014).

623 60 Arai, M., Sugase, K., Dyson, H. J. & Wright, P. E. Conformational propensities of intrinsically disordered proteins influence the mechanism of binding and folding. *Proc Natl Acad Sci U S A* **112**, 9614-9619, doi:10.1073/pnas.1512799112 (2015).

626 61   Oldfield, C. J. & Dunker, A. K. Intrinsically disordered proteins and intrinsically disordered
627   protein regions. *Annu Rev Biochem* **83**, 553-584, doi:10.1146/annurev-biochem-072711-164947
628   (2014).
629 62   Ezerski, J. C., Zhang, P., Jennings, N. C., Waxham, M. N. & Cheung, M. S. Molecular Dynamics
630   Ensemble Refinement of Intrinsically Disordered Peptides According to Deconvoluted Spectra
631   from Circular Dichroism. *Biophysical journal* **118**, 1665-1678, doi:10.1016/j.bpj.2020.02.015
632   (2020).
633 63   Choi, U. B. *et al.* Modulating the intrinsic disorder in the cytoplasmic domain alters the biological
634   activity of the N-methyl-D-aspartate-sensitive glutamate receptor. *J Biol Chem* **288**, 22506-
635   22515, doi:10.1074/jbc.M113.477810 (2013).
636 64   Choi, U. B., Xiao, S., Wollmuth, L. P. & Bowen, M. E. Effect of Src kinase phosphorylation on
637   disordered C-terminal domain of N-methyl-D-aspartic acid (NMDA) receptor subunit GluN2B
638   protein. *J Biol Chem* **286**, 29904-29912, doi:10.1074/jbc.M111.258897 (2011).
639 65   Zeng, W. Z., Liu, D. S. & Xu, T. L. Acid-sensing ion channels: trafficking and pathophysiology.
640   *Channels (Austin)* **8**, 481-487, doi:10.4161/19336950.2014.958382 (2014).
641 66   Hruska-Hageman, A. M., Wemmie, J. A., Price, M. P. & Welsh, M. J. Interaction of the synaptic
642   protein PICK1 (protein interacting with C kinase 1) with the non-voltage gated sodium channels
643   BNC1 (brain Na+ channel 1) and ASIC (acid-sensing ion channel). *Biochem J* **361**, 443-450,
644   doi:10.1042/0264-6021:3610443 (2002).
645 67   Zha, X. M. *et al.* ASIC2 subunits target acid-sensing ion channels to the synapse via an
646   association with PSD-95. *J Neurosci* **29**, 8438-8446, doi:10.1523/JNEUROSCI.1284-09.2009
647   (2009).
648 68   Price, M. P., Thompson, R. J., Eshcol, J. O., Wemmie, J. A. & Benson, C. J. Stomatin
649   modulates gating of acid-sensing ion channels. *J Biol Chem* **279**, 53886-53891,
650   doi:10.1074/jbc.M407708200 (2004).
651 69   Meng, H. *et al.* Death-domain dimerization-mediated activation of RIPK1 controls necroptosis
652   and RIPK1-dependent apoptosis. *Proceedings of the National Academy of Sciences* **115**,
653   E2001-E2009, doi:10.1073/pnas.1722013115 (2018).
654

Supplemental Figures
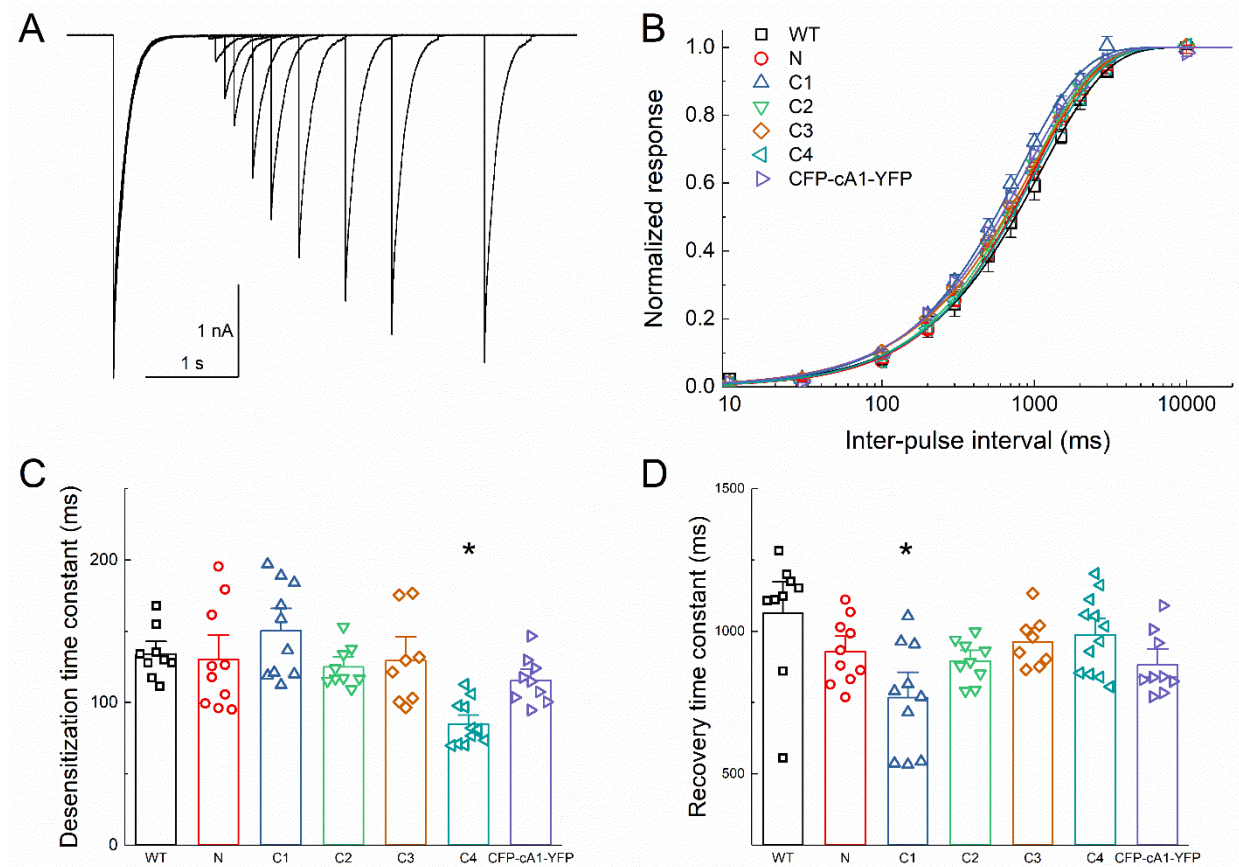
Supplemental Figure 1
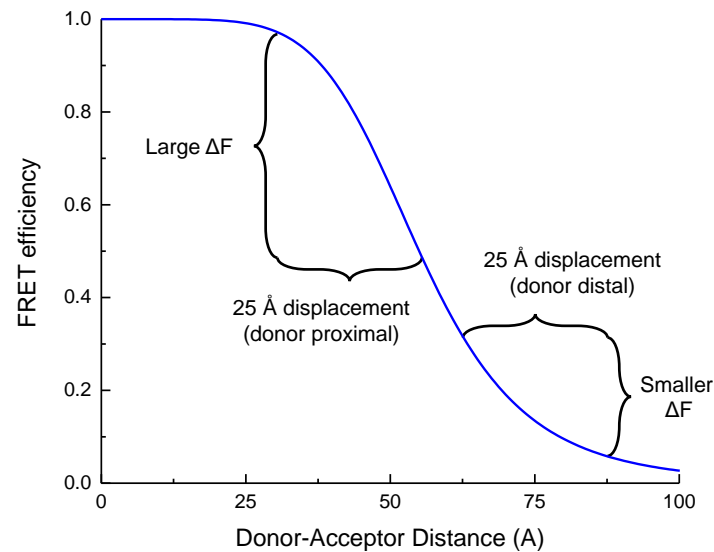
Supplemental Figure 1: Non-linearity of FRET provides for distance estimates. Simulated FRET efficiency over distance with an R_0 of 55 angstroms. Moving donor and acceptor apart by a fixed distance has a larger effect when the donor and acceptor are close (donor proximal case) compared to when they are further apart (donor distal case).

Supplemental Figure 2
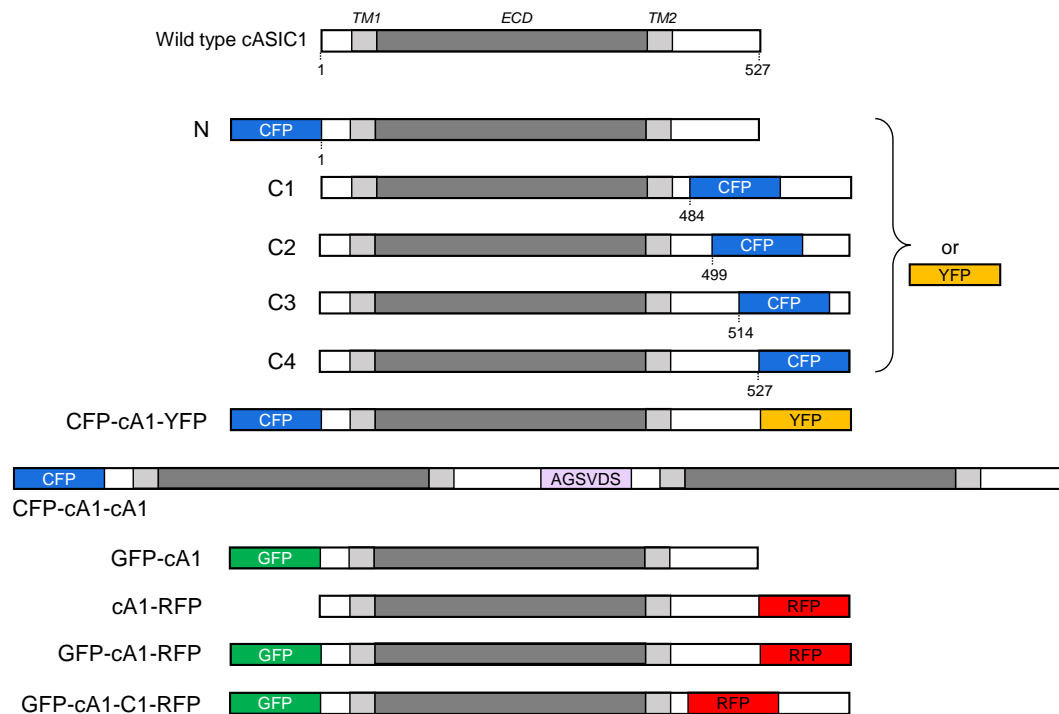
Supplemental Figure 2: cASIC1 constructs used in this study. The extracellular domain (*ECD*) and transmembrane helices (*TM*) are grey with amino and carboxy termini depicted in white. Numbers indicate the amino acid position for insertion. The violet bar shows the amino acid linker between the first and second subunit in the cASIC1 dimer. CFP, YFP, GFP and RFP represent mTurq2, mVenus, Gamillus and tagRFP, respectively. See *Methods* for further details.
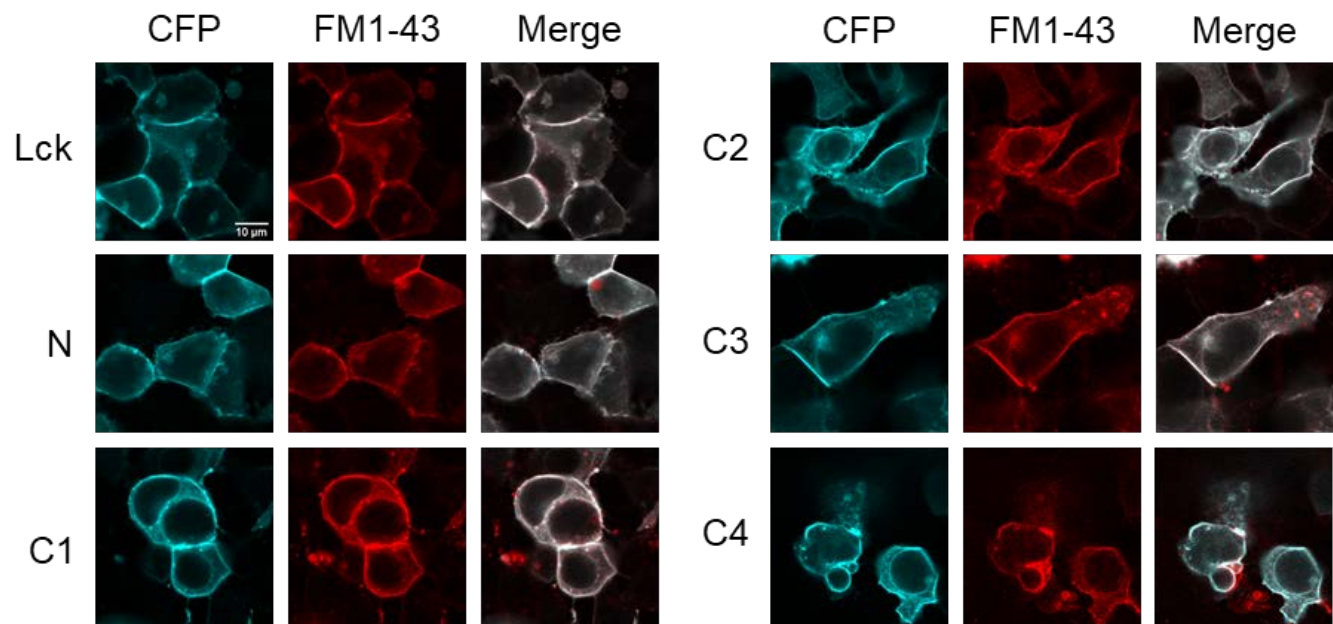
Supplemental Figure 3

Supplemental Figure 3: FP insertion does not substantially alter desensitization kinetics.
(A) Outside-out patch recording of cASIC1 CFP at C3 during paired pulse stimulation protocol using pH 8 and pH 5. **(B)** Recovery from desensitization curves over various inter-pulse intervals for the indicated constructs. **(C & D)** Summary of desensitization entry **(C)** and recovery **(D)** time constants for the indicated constructs. Symbols denote individual excised patches (N = 9 – 12 patches per construct). Asterisks indicate significant difference compared to wild type using randomization test. For C4 desensitization, p = 0.025. For C1 recovery, p = 0.0073. Error bars represent SEM in all panels.
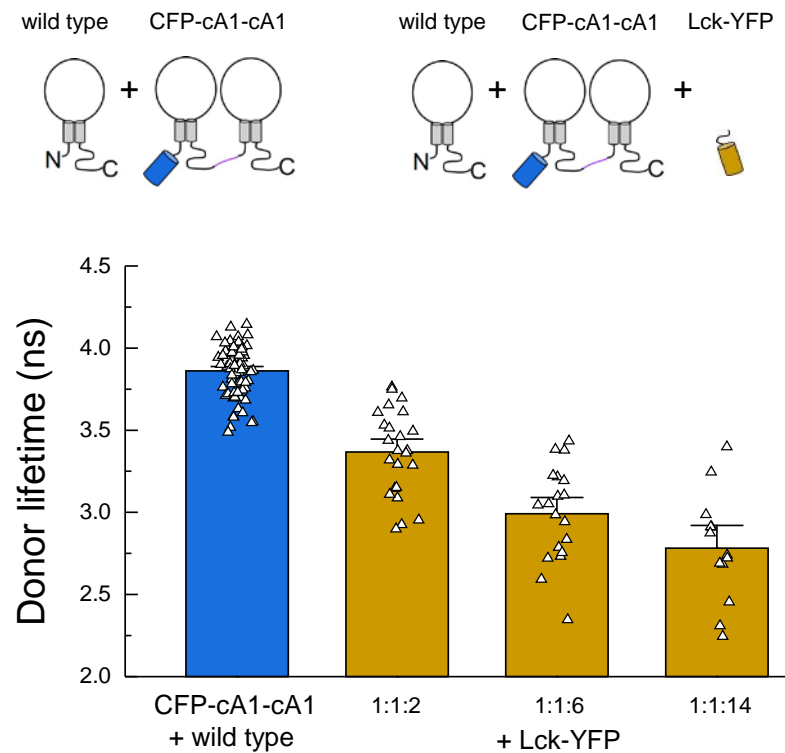
Supplemental Figure 4

Supplemental Figure 4: Lck-CFP and CFP-tagged cASIC1 constructs localize to the plasma membrane. Confocal images of HEK293T cells transfected with the indicated constructs two days prior. Plasma membrane was stained with FM1-43 (5 μM) immediately prior to imaging.
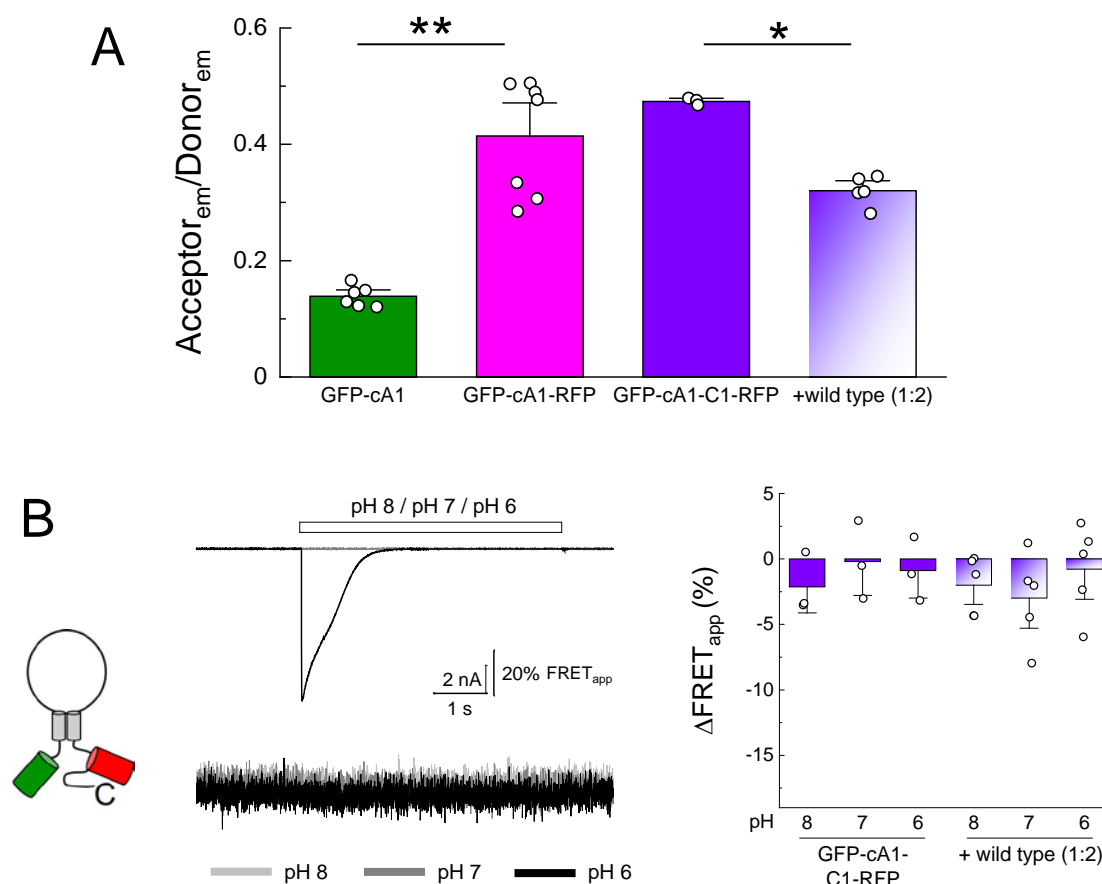
Supplemental Figure 5
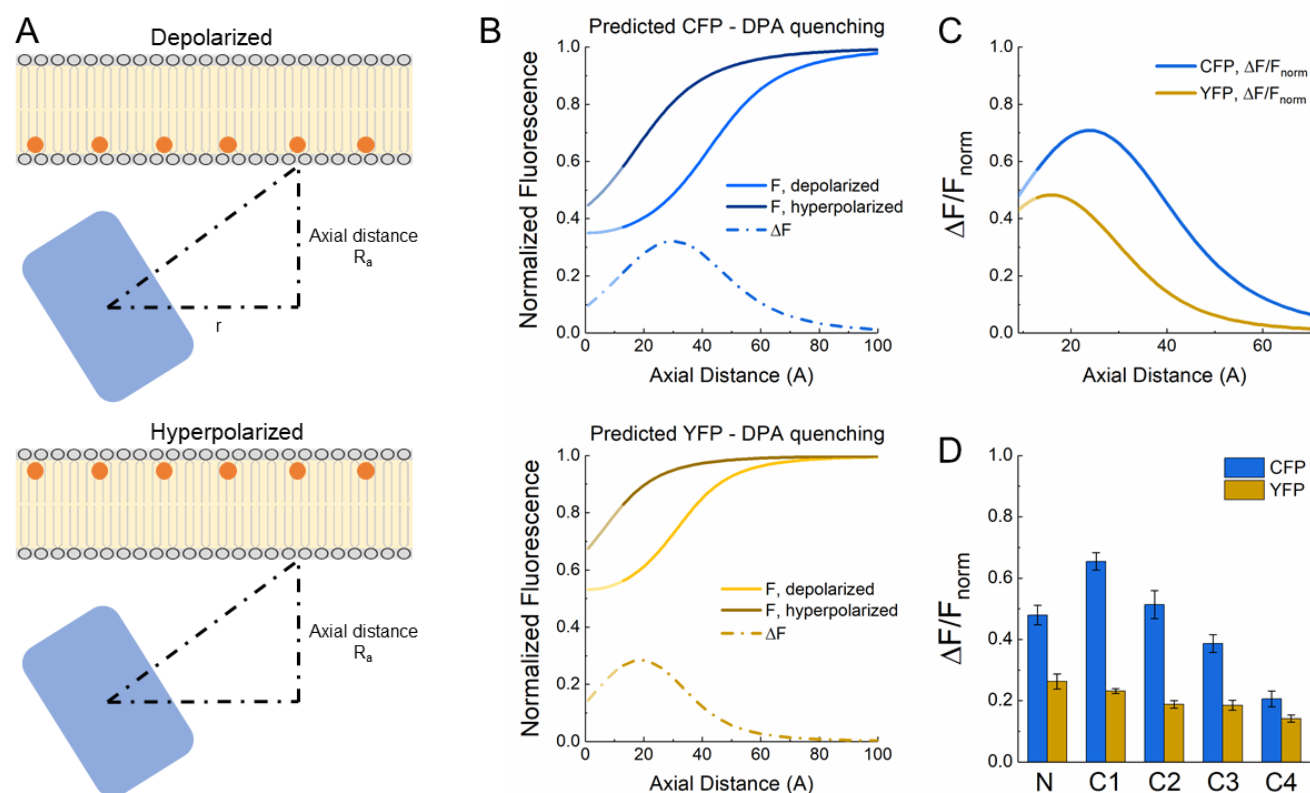
Supplemental Figure 5: Theoretical analysis of FP-DPA quenching. (A) Schematic of DPA quenching of a fluorophore positioned away from the plasma membrane. **(B)** Predicted quenching curves for CFP (*upper*) and YFP (*lower*) at depolarized (*light color*) or hyperpolarized (*darker color*) voltages. Dotted line depicts the difference between hyperpolarized and depolarized curves or ΔF as a function of axial distance. **(C)** ΔF versus distance curves normalized to fluorescence at hyperpolarized voltage or $\Delta F/F_{norm}$ as a function of distance. **(D)** Plot of observed quenching (ie. $\Delta F/F_{norm}$) for each FP insertion. Same data as in Figure 2D. Note similarity with predicted $\Delta F/F_{norm}$ curves in panel **C**.

Supplemental Figure 6

Supplemental Figure 6: FRET due to membrane 'crowding'. Cartoon (*upper*) and lifetimes (*lower*) from the indicated constructs for measuring FRET between cASIC dimer and membrane tethered YFP (Lck-YFP) over varying cDNA ratios. Symbols denote single cells (N = 13 – 74 cells per construct) and error bars are SEM
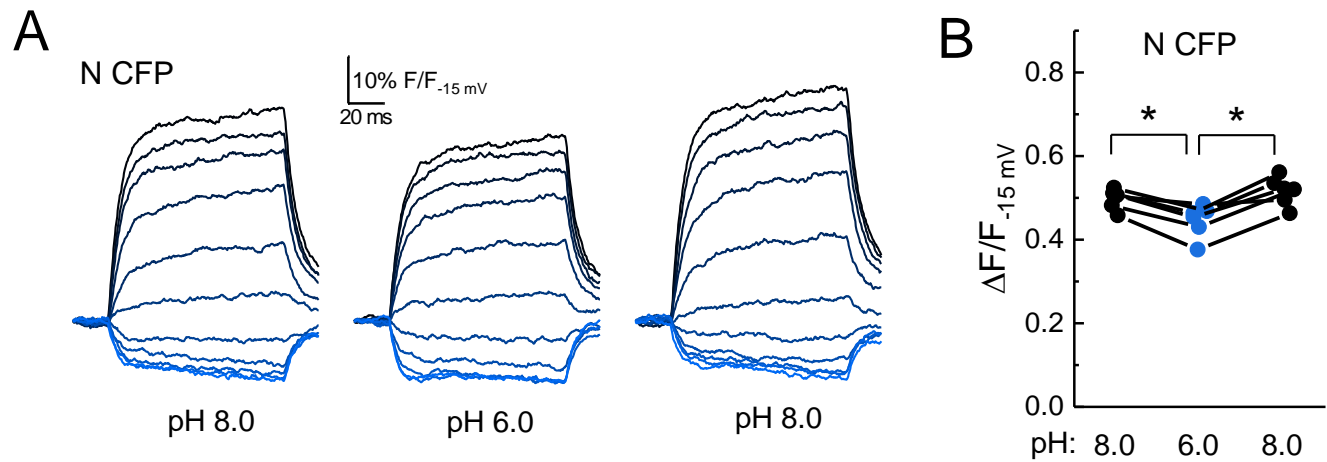
Supplemental Figure 7

Supplemental Figure 7: N and C terminal GFP and RFP do not change FRET efficiency upon extracellular acidification. (A) Summary of green fluorescence emission divided by red fluorescence emission upon GFP excitation for the indicated clones. ** denotes p = 0.0007, * indicates p = 0.0121 by randomization test. **(B)** Cartoon (*left*), example traces of current and fluorescence ratio (*middle*) and summary changes to apparent FRET (*right*) from the indicated. Symbols denote single cells (N = 3 – 7 cells per construct) and error bars are SEM.

Supplemental Figure 8

Supplemental Figure 8: Extracellular acidification-induced motion of N CFP is readily reversible. (A) Fluorescence-voltage traces from single cell expressing N CFP in the indicated extracellular buffer with 5 μM DPA. **(B)** Summary of the voltage-dependent extent of DPA quenching from N CFP in the indicated extracellular pH. Symbols denote individual cells (N = 5) and error bars represent SEM. * indicates p value < 0.05 by Wilcoxon rank sum test.